Original Article

Synthesis of Fe-Ni-doped graphene electrocatalyst for hydrogen evolution reaction via UV-assisted phytochemical reduction using *Andrographis paniculata* extract

Keessha Shamae A. Cham[1], Julius D. Belesario[1], Veronica V. Blanca[1], Amyrie R. Galut[1], Rugi Vicente C. Rubi[1], and Jonyl L. Garcia[2*]

[1] Department of Chemical Engineering, College of Engineering,
Adamson University, Manila, 1000 Philippines

[2] Department of Chemistry, College of Science,
Adamson University, Manila, 1000 Philippines

Abstract

Electrocatalytic water-splitting is a promising method for hydrogen production. Fe-Ni-doped graphene (Fe-Ni-G) for hydrogen evolution reaction (HER) was synthesized via UV-assisted phytochemical reduction using *Andrographis paniculata* extract (*AP*). The impact of *AP* mass loading and UV irradiation time on Fe-Ni-G's electrocatalytic activity towards HER was explored. FTIR and SEM-EDX characterizations confirmed the successful reduction and incorporation of Fe and Ni on the graphene surface. The onset potential for HER on Fe-Ni-G ranged from -0.632 V to -0.548 V (vs. SHE). Optimizing *AP* mass loading and UV time yielded the best results with 5 g *AP* and 1 h UV irradiation producing the highest H_2 gas evolution (~3.4 mL) after 1 h electrolysis in 0.5 M H_2SO_4 at 3 V. This study suggests a cost-effective and eco-friendly route for preparing HER electrocatalysts through UV-assisted phytochemical reduction using *AP* as a reducing agent.

Keywords: phytochemical reduction, electrocatalyst, hydrogen evolution reaction, green chemistry, graphene

1. Introduction

In today's energy transition structure, hydrogen gas is seen as an essential commodity and a greener and renewable energy source (Rubi *et al.,* 2020). Hydrogen gas is commonly produced from the steam reforming of hydrocarbons, alcohols, and natural gas, which entails dependence on nonrenewable fossil fuels (Kumar, Vikrant, Younis, & Kim, 2023). A greener alternative would be to produce H_2 gas via electrochemical water splitting. However, this process requires large amounts of energy (E = 1.23 V) usually with a low yield (Sapountzi, Gracia, Weststrate, Fredriksson, & Niemantsverdriet, 2017).

To address the problem, researchers have developed new materials for electrocatalysts in the hydrogen evolution half of the water-splitting reaction (Dues, C., Schmidt, W. G., & Sanna, S., 2019; Khan, Kamal, Asiri, & Bakhsh, 2021). Platinum is the standard, but it's expensive and scarce. Transition metals like Fe and Ni are promising alternatives. Yan *et al.* (2016) found high electrocatalytic activity in $FeNi_3/NiFeO_x$ nanohybrids, with a small onset potential of ~20 mV due to synergy. Lian *et al.* (2018) reported a Ni-Fe alloy with a small onset potential of –286 mV vs. RHE. Using chemical reducing agents generates hazardous waste, contradicting the eco-friendly energy production goals. Carbon black as a support matrix limits surface area and reduces H_2 production efficiency (Sapountzi, Gracia, Weststrate, Fredriksson, & Niemantsverdriet, 2017).

Phytochemical reduction, a green chemistry method for making metal particles, stands out due to its simplicity, cost-

---

*Corresponding author
Email address: jonyl.garcia@adamson.edu.ph

effectiveness, and safety. Phytochemical extracts, often derived from waste or non-edible plants, contain agents like phenolic compounds, flavonoids, and alkaloids (Sundrarajan & Muthulakshmi, 2021). These compounds reduce and protect, yielding metallic micro- and nano-particles (Nguyen *et al.*, 2022). In a recent study by Watcharaporn, Opaprakasit, and Pimpan (2014), silver nitrate reduction by tannic acid under UV radiation at room temperature led to spherical, size-varying silver nanoparticles at different pH levels. Synthesizing platinum-carbon catalysts using various reducing agents under UV light increased the electrochemically active surface area by 80% by reducing platinum NP size and enhancing their spatial distribution (Paperzh *et al.*, 2021).

Graphene, a monoatomic-thick 2-D carbon allotrope, is well-known for its high electrical conductivity, surface area, and mechanical strength (Zhan, Lei, & Zhang, 2022). These properties make it an ideal support matrix for carbon-based electrocatalysts (Tiwari, Sahoo, Wang, & Huczko, 2020). In Badrayyana *et al.*'s (2015) study, adding graphene to an electrolyte bath led to porous 3D nano-sized Fe-Ni spheres on graphene, enhancing the electrochemically active surface area. In another study by Cui *et al.* (2018), they synthesized quaternary $Co_{0.8}Ni_{0.1}Fe_{0.1}S_2$ nanoparticles grown on reduced graphene oxide (CNFS@rGO) with high HER performance: an overpotential of 138 mV for 10 mA cm^{-2} and a Tafel slope of 49 mV/dec.

In this study, we present a novel approach to synthesizing Fe-Ni-doped graphene (Fe-Ni-G) via UV-assisted phytochemical reduction using the ethanolic extract of *Andrographis paniculata* (*AP*), commonly known as "serpentina". *AP* is a potential medicinal plant that belongs to the *Acanthaceae* family, abundant in India, China, and Sri Lanka, and is utilized for addressing respiratory infections, malaria, and various inflammatory conditions. Previous studies have shown that serpentina contains phytochemicals such as flavonoids, polyphenols, and terpenoids, which are potent reducing agents. Specifically, the effect of *AP* mass loading and UV irradiation time on the performance of the resulting electrocatalyst towards HER is presented.

2. Materials and Methods

2.1 Reagents and precursors

The leaves and stems of *Andrographis paniculata* were harvested from Novaliches, Quezon City, Philippines. Expanded graphite (EG; 200 mesh, 99% purity, Jinglong Special Carbon Technology Co., Ltd., Beijing, China) and N-methyl-2-pyrrolidone (NMP) (C_5H_9NO, 99% purity, Jinan Future Chemical Co., Ltd., China) were used to produce exfoliated graphene via liquid phase shear exfoliation (LPSE). Iron (III) nitrate nonahydrate ($Fe(NO_3)_3 \cdot 9H_2O$, ≥98% purity, Jinan Future Chemical Co., Ltd., China) and nickel (II) nitrate hexahydrate ($Ni(NO_3)_2 \cdot 6H_2O$, ≥98.0% purity, Jinan Future Chemical Co., Ltd., China) were used as Fe and Ni precursors, respectively.

Nafion solution (5%, D-521, Owl Materials Technology, Shenzhen, China) and ethanol (AR grade) were used to prepare catalyst inks. All aqueous solutions were prepared using ultrapure water (r = 18.2 Ω·cm).

2.2 Preparation of *AP* ethanolic extract

The leaves and stems were washed, cleaned, and dried in a convection oven at 40 °C. The particle sizes of the dried *AP* stems and leaves were reduced to 50 mesh (300 microns) using a food-grade blender. The powdered *AP* was stored in an airtight container and kept in a refrigerator (4 °C) before use.

Samples of powdered and dried *AP* were transferred into an Erlenmeyer flask and were mixed with 50% (v/v) ethanol-water solution at 5 g *AP* per 200 mL extracting solution. The mixture was then placed on an orbital shaking water bath set at 30 °C and 240 rpm for 2 hours. The resulting mixture was filtered, with the filtrate stored in an air-tight container and stored in a refrigerator before use.

2.3 Liquid-phase shear exfoliation (LPSE) of expanded graphite (EG)

LPSE was carried out using an overhead stirrer to exfoliate the expanded graphite with NMP at 120 rpm. A 10 g EG was exfoliated for 1 h in 700 ml NMP. The exfoliated dispersions were centrifuged at 3200 rpm for 30 min, and the resultant supernatant was collected. The synthesized graphene was dried in a freeze dryer (- 79 °C) for approximately 3 hours. When compared to the exfoliation of natural flake graphite (NFG), the LPSE of EG in NMP is known to provide better yields, as much as six times higher than NFG (Ghanbari, Shafikhani, & Daryalaal, 2019).

2.4 Preparation of Fe-Ni-doped graphene (Fe-Ni-G)

Hydrothermal and carbonization methods were used to synthesize Fe-Ni-doped graphene (Fe-Ni-G). Briefly, 100 mg of graphene was dispersed in 50 ml of ultrapure water and then sonicated for 30 minutes. Afterward, 1.8 mmol of iron (III) nitrate nonahydrate, 12.5 mmol of nickel (II) nitrate hexahydrate, and x g/ml of *AP* (x = 0.025, 0.050, and 0.075) were added to the above solution while stirring and as it was exposed to UV light. Three trials were conducted at varying UV exposure times (1 h, 3h, and 5 h). After stirring, the mixtures were placed into a Teflon-lined autoclave and heated at 120 °C for 6 hours. Suction filtration was used to collect the resulting black mass, which was then washed multiple times with water and ethanol to remove the unreacted *AP* phytoconstituents before being dried in an oven at 100 °C for 2 hours. Lastly, the samples were carbonized in a muffle furnace at 800 °C for 2 hours to produce the final Fe-Ni-G product.

2.5 Materials characterization

The surface morphology and elemental composition of Fe-Ni-G were studied using scanning electron microscope – energy dispersive x-ray device (SEM-EDX, Phenom XL, Thermo Scientific) equipped with a back-scattered electron detector. On the other hand, spectroscopic analysis was done using a Fourier transform infrared spectrometer (Spectrum Two, Perkin Elmer) equipped with a diamond crystal over the scan range from 4000 cm^{-1} to 550 cm^{-1}.

2.6 Electrochemical characterization

2.6.1 Preparation of a catalyst electrode

In a 1 ml solution of 200 µL of ethanol and 800 µL of distilled water, 1 mg of catalyst and 80 µL of Nafion solution (5 %wt.) were dispersed *via* sonication for 1 h. Then, 35 µL of catalyst slurry was drop cast onto the surface of a polished glassy carbon electrode (φ: 3mm) to generate a catalyst loading of 0.50 mg/cm^2.

2.6.2 Linear sweep voltammetry

The as-prepared Fe-Ni-G was also characterized using linear sweep voltammetry (LSV) in 0.5 M H_2SO_4. All the experimental data were calibrated with reference to a standard hydrogen electrode (SHE) using equation (1):

$$E_{SHE} = E_{Ag/AgCl} + E^0_{Ag/AgCl} + 0.059\ pH \quad (1)$$

In this equation, $E_{Ag/AgCl}$ is the observed potential, while experiments were performed using an Ag/AgCl (3M KCl) reference electrode. $E^0_{Ag/AgCl}$ is the potential of Ag/AgCl (in 3M KCl) vs. (SHE), i.e., 0.197 V. LSV was performed at potential range between 0 V and – 0.8 V at a scan rate of 2 mV·s^{-1}.

Tafel plots were generated by fitting the LSV data into the Tafel equation (2):

$$\eta = b\ log(j_0) + a \quad (2)$$

where η is the overpotential, j_0 is the exchange current density, and b is the Tafel slope. Before LSV, nitrogen gas (purity: 99.999%) was bubbled into the aqueous solution for 15–20 minutes to remove any dissolved oxygen.

2.6.3 H_2 gas evolution experiments

Estimating the hydrogen gas evolved using the as-prepared Fe-Ni-G electrocatalysts as the cathode in electrolysis of the 0.5 M H_2SO_4 aqueous solution was done using an improvised electrolysis setup. Graphite rods (φ: 10 mm) were used as electrodes. The cathode electrode was insulated to expose only the tip where the electrocatalyst ink (from Section 2.6.1) was drop cast to a catalyst loading of 0.23 mg/cm^2. Two 1.5 V dry cell batteries, connected in series to reach 3 V, were used as the power supply for the electrolysis experiment. The electrolysis was performed for 1 h, with the H_2 gas collected using an inverted graduated cylinder filled with 0.5 M H_2SO_4. The volume of H_2 gas collected was estimated using the water displacement method.

3. Results and Discussion

3.1 Morphological and elemental characterization

SEM-EDX was used to determine Fe-Ni-G HER electrocatalyst surface morphology (Figure 1) and elemental composition (Table 1). The influence of UV irradiation time on Fe-Ni-G morphology, prepared with 15 g AP, is illustrated. Pristine graphene (Figure 1 (a)) exhibited a typical wrinkled sheet-like morphology (Garcia, Miyao, Inukai, & Tongol,
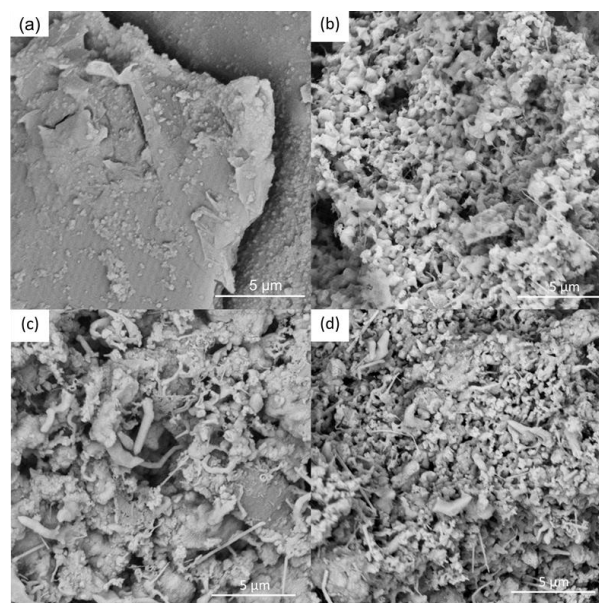

Figure 1. SEM images for (a) pristine graphene at 16,000× magnification; Fe-Ni/G-15g*AP* nanocomposites prepared via UV irradiation for (b) 1 h, (c) 3 h, and (d) 5 h, at 15,000× magnification

Table 1. Elemental analysis

| Element	Sample			
	a	b	c	d
Fe	-	20.10	26.84	25.58
Ni	-	10.11	9.03	20.35
C	86.40	2.37	5.57	11.42
O	13.60	67.42	58.56	42.65

2022). UV-assisted reduction of Fe and Ni using AP at varying UV times produced different morphologies (Figure 1 (b-d)), suggesting that agglomeration increased with UV time.

Iron-based catalysts exhibit low-overpotential HER activity and a high active surface area, facilitating effective catalysis (Khan *et al.*, 2021). Nickel nanoparticles efficiently produce hydrogen due to low energy barriers and high catalytic activity (Huo *et al.*, 2022). The Fe/Ni ratio significantly influences electrocatalyst performance, catalytic activity, electronic structure, surface properties, and active sites.

Optimizing the Fe/Ni ratio can result in improved HER kinetics and increased catalytic activity (Heo *et al.*, 2023). In acidic media, HER occurs via a two-step process (Park *et al.*, 2022). Initially, H$^+$ ions are adsorbed on the electrocatalyst surface via the Volmer reaction as in (3):

$$H^+ + e^- \rightarrow H_{ads} \quad (3)$$

The subsequent release of H_2 gas follows either a Heyrovsky (4) or a Tafel (5) process:

$$H^+ + e^- + H_{ads} \rightarrow H_{2(g)} \quad (4)$$

$$2H_{ads} \rightarrow H_{2(g)} \quad (5)$$
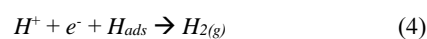
While both processes are two-electron reduction reactions, the Volmer-Heyrovsky is known to be more prevalent over the Volmer-Tafel route, with the latter's rate constant neglected in most cases (Park *et al.*, 2022). Investigation using scanning electrochemical microscopy by Liang and co-workers showed that the Volmer reaction is the rate-limiting step for HER (Liang *et al.*, 2017). On Ni-modified surfaces, the electrocatalytic activity of HER is enhanced due to the presence of nickel oxide species (Liang *et al.*, 2017). These surface oxides provide anchor sites for the adsorption of H^+, promoting further the rate-limiting Volmer reaction. Combining Fe with Ni was shown to further enhance HER by expanding the coverage of these surface oxides since Fe is more oxophilic than Ni (He *et al.*, 2020). Optimizing the Fe-Ni ratio takes advantage of this solid synergistic interaction towards HER.

EDX analysis (Table 1) revealed that UV irradiation time was able to influence significantly the Fe:Ni ratio of the resulting Fe-Ni-G. At UV irradiation times of 1 h, 3 h, and 5 h, the Fe:Ni mass ratios were estimated as 2:1, 3:1, and 5:4, respectively. The higher Fe content for all of the Fe-Ni-G relative to the Ni content could be attributed to the more positive reduction potential Fe relative to Ni, which makes the former easier to reduce. Increasing the UV irradiation time from 1 h to 5 h resulted in the doubling of the Ni content, which shows the effectiveness of UV irradiation in promoting metal ion reduction with *AP* extract. UV irradiation of phytochemicals from plant extracts produced more potent reducing agents, such as gallic acid, which enhanced metal ion-reducing capability (Watcharaporn, Opaprakasit, & Pimpan, 2014). However, longer UV exposure can lead to increased particle agglomeration, affecting HER electrocatalyst performance (Zhong, Wang, Guo, & Tang, 2013). This may be due to surface defect formation and enhancing catalytic activity, leading to a high electrocatalytic performance. Additionally, creating smaller anisotropic particles increases the available active surface area, favoring catalytic activity (Boudet *et al.*, 2022).

3.2 Spectroscopic characterization

FTIR spectroscopy (Figure 2) identified surface functionalities in Fe-Ni-G. Pristine graphene (Figure 2, yellow trace) displayed bands at 1720 cm^{-1} (C=O) and 1590 cm^{-1} (C=C) (Garcia, Miyao, Inukai, & Tongol, 2022) and a broad 3300 cm^{-1} band (–OH), indicating graphene oxide from the LPSE process, consistent with previous studies (Ghanbari, Shafikhani, & Daryalaal, 2019).

Dried AP extract's IR bands (Figure 2, gray trace) included 3300 cm^{-1} (–OH), 2909 cm^{-1} (sp^3 C-H), 2841 cm^{-1} (aldehydic C-H), 1599 cm^{-1} (C=O), and 1022 cm^{-1} (C-O), attributed to various phytochemicals like flavonoids, phenols, and terpenoids (Sangeetha, Archit, & SathiaVelu, 2014) known for their role as reducing agents (Nguyen *et al.*, 2022). Flavonoids in AP actively bind and convert metal ions into metallic particles, and UV exposure enhances their reducing power (Khan *et al.*, 2021). Carbonization exposes active sites for HER electrocatalysis. The appearance of a strong 596 cm^{-1} band in Fe-Ni-G (Figure 2, red, blue, and green traces) confirmed successful Fe-O and Ni-O species incorporation (Nandiyanto, Oktiani, & Ragadhita, 2019; Wongsa, Phatikulrungsun, & Prathumthong, 2022). Bands at 2978 cm^{-1}

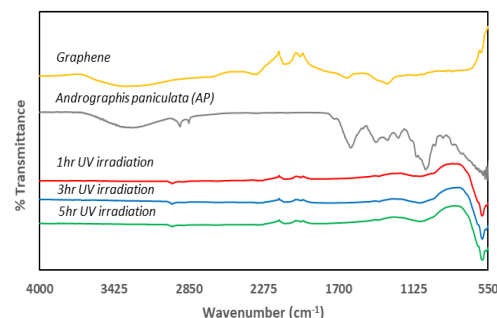Figure 2. FTIR spectral profiles of graphene, *AP*, and FeNi/G (*AP* mass loading 15 g) irradiated with UV for various times.

(sp^3 C-H) and 1068 cm^{-1} (C–O) arise from carbonized AP extract constituents acting as reducing and capping agents for Fe^{3+} and Ni^{2+}. Overall, FTIR indicates successful Fe-Ni-G electrocatalyst production.

3.3 Electrochemical measurements

The overpotential gauges measure the potential (voltage) needed to overcome kinetic barriers in HER, indicating catalyst efficiency (Stratakes, Dempsey, & Miller, 2021). This is the difference between onset and equilibrium potentials. Lower overpotential signifies better HER efficiency and higher electrocatalyst activity. Onset potential marks HER commencement, with lower values indicating a more active catalyst (Botz, Nebel, Rincón, Ventosa, & Schuhmann, 2015). Figure 3 displays LSV curves for H_2 evolution by Fe-Ni-G catalysts in 0.5 M H_2SO_4. At 0.50 mg·cm^{-2} electrocatalyst loading, onset potentials ranged from –0.500 V to –0.650 V at 2 mV·s^{-1} scan rate, allowing HER overpotential estimation. Table 2 shows how AP mass loading and UV time influenced Fe-Ni-G onset potentials. For 1 h and 3 h UV exposure, 5 g AP gave the lowest onset potentials at –0.589 V and –0.548 V, while at 5 h UV exposure, 10 g AP yielded the lowest onset potential at –0.573 V.

Tafel slopes in Figure 4 and Table 2 evaluate HER kinetics. Smaller Tafel slopes in the Tafel region indicate a faster rate-determining step, potentially related to hydrogen atom/ion recombination (Paul, Sreekanth, Biroju, Narayanan, & Giri, 2018). Tafel slope increased with higher AP mass loading and longer UV exposure from 335.92 mV/dec (5-g AP) to 408.72 mV/dec (15-g AP) for 5-h UV exposure, implying increased activation energy for H atom/ion recombination. AP mass loading affects phytochemical concentration, acting as reducing and capping agents for Fe and Ni. UV exposure influences phytochemical kinetics (Gopalakrishnan, Radha, & Devasena, 2019; Paperzh *et al.*, 2021). Flavonoids in AP bind to and reduce metal ions into particles, while metal ion content and entry points shape particle size and form (El-Seedi *et al.*, 2019). Varying process parameters alter particle form, dispersion, and yield, creating more active HER sites. UV exposure activates phyto chemicals, forming reactive catalyst surface species (Khan *et al.*, 2021). Increased Tafel slopes at higher AP mass loading block HER sites due to more capping agents (Campisi, Schiavoni, Chan-Thaw, & Villa, 2016). The same trend occurs with longer UV exposure, leading to particle agglomeration and decreased HER surface area (Duan *et al.*, 2021).
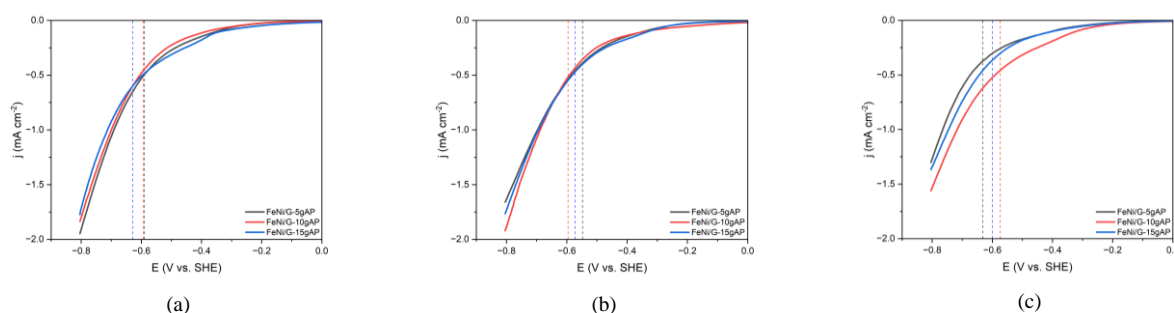
| (a) | (b) | (c) |

Figure 3.   LSV polarization curves for Fe-Ni-G prepared by UV irradiation at (a) 1 h, (b) 3 h, and (c) 5 h. Electrolyte 0.5 M H_2SO_4; scan rate 2 mV·s^{-1}.
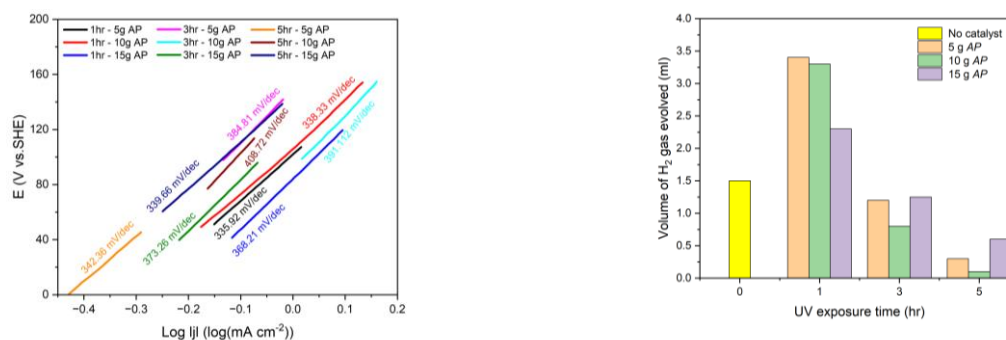

Figure 4.   Tafel slopes for Fe-Ni-G prepared with various UV irradiation times and *AP* mass loadings.

Figure 5.   Effect of *AP* mass loading and UV exposure time on the volume of H_2 gas evolved in electrolysis of 0.5 M H_2SO_4 at 3 V for 1 h.

Table 2.   Onset potential and Tafel slope for FeNi/G electrocatalysts prepared at varying *AP* mass loadings and UV irradiation times.

Irradiation time (hr)	*AP* mass loading (g)	Onset potential (V)	Tafel slope (mV/dec)
1	5	-0.589	335.92
	10	-0.594	338.33
	15	-0.629	368.21
3	5	-0.548	384.81
	10	-0.596	391.12
	15	-0.572	373.26
5	5	-0.632	342.36
	10	-0.573	408.72
	15	-0.600	339.66

3.4 Results of the H₂ evolution experiments

Figure 5 summarizes H_2 gas volume in an improvised electrolysis setup (Section 2.6.3). Fe-Ni-G outperformed bare graphite electrodes at 3 V for 1 h, producing more H_2 gas (2.3 mL vs. 3.4 mL). Electrocatalysts aid water splitting by providing active sites for water molecule adsorption and activation. Fe and Ni's redox properties and catalytic activity make them popular HER electrocatalyst components (Hu *et al.*, 2019). Adding graphene as a support material enhances electron transfer and catalyst stability (Ahmad, Fan, & Hui, 2018), improving the hydrogen evolution process.

Figure 5 also shows that lower AP mass loading and shorter UV exposure led to more H_2 gas from Fe-Ni-G. This relates to mass transfer limitations caused by excessive
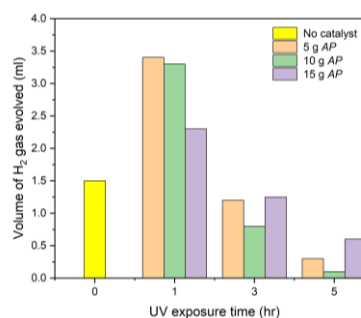
material covering Fe and Ni particles (Zhang, Xu, Han, Tian, & Jiang, 2023; Zuo, Su, & Yan, 2023). These findings align with electrochemical data. Specifically, the Fe-Ni-G from 5 g AP and 1 h UV exposure, with the lowest Tafel slope (Table 2), produced the most H_2 gas (~3.4 mL) (Figure 5). SEM data showed this Fe-Ni-G had the least particle agglomeration (Figure 1 (b)). The Fe:Ni ratio (2:1) in this Fe-Ni-G enhanced electrocatalytic activity for HER. This emphasizes the significance of the Fe:Ni ratio, agglomeration, and surface exposure in Fe-Ni-G electrocatalyst effectiveness for HER.

Improved H_2 evolution efficiency with Fe-Ni-G has significant implications for renewable energy and hydrogen storage. It could advance cleaner, sustainable energy technologies, promoting hydrogen's role in the future energy landscape. Enhancing Fe-Ni-G performance via UV-assisted phytochemical reduction should focus on parameter control and optimization.

4. Conclusions

This study provided the first-time preparation of Fe-Ni-G *via* UV-assisted phytochemical reduction using the ethanolic extract of the plant *Andrographis paniculata*. A low *AP* mass loading (5 g) and short UV irradiation time (1 h) gave the best-performing Fe-Ni-G HER electrocatalyst, which produced as much as ~3.4 mL H_2 gas in 1 h of electrolysis at 3 V. This matches the data obtained from electrochemical and materials characterizations.

We recommend optimizing the synthesis parameters for further studies using the "design of experiments" approach. Moreover, further characterization, such as x-ray photoelectron spectroscopy, could reveal more profound

insights into the nature of the HER active sites on the prepared Fe-Ni-G.

References

Ahmad, H., Fan, M., & Hui, D. (2018). Graphene oxide incorporated functional materials: A review. *Composites Part B: Engineering*, *145*(1), 270–280. doi:10.1016/j.composites.2018.02

Badrayyana, S., Bhat, D. K., Shenoy, S., Ullal, Y., & Hegde, A. C. (2015). Novel Fe-Ni-Graphene composite electrode for hydrogen production. *International Journal of Hydrogen Energy, 40*(33), 10453–10462. Retrieved from https://doi.org/10.1016/j.ijhydene.2015.06.040

Boudet, A., Henrotte, O., Limani, N., Orf, F. E., Oswald, F., Jousselme, B., & Cornut, R. (2022). Unraveling the link between catalytic activity and agglomeration state with scanning electrochemical microscopy and atomic force microscopy. *Analytical Chemistry*, *94*(3), 1697-1704. Retrieved from https://doi.org/10.1021/acs.analchem.1c04256

Botz, A. J. R., Nebel, M., Rincón, R. A., Ventosa, E., & Schuhmann, W. (2015). Onset potential determination at gas-evolving catalysts by means of constant-distance mode positioning of nano electrodes. *Electrochimica Acta, 179*, 38–44. Retrieved from https://doi.org/10.1016/j.electacta.2015.04.145

Campisi, S., Schiavoni, M., Chan-Thaw, C. E., & Villa, A. (2016). Untangling the role of the capping agent in nanocatalysis: Recent advances and perspectives. *Catalysts, 6*(12), 1–21. Retrieved from https://doi.org/10.3390/catal6120185

Cui, Y., Zhang, R., Zhang, J., Wang, Z., Xue, H., & Mao, W. (2018). Highly active and stable electrocatalytic hydrogen evolution catalyzed by nickel, iron doped cobalt disulfide @reduced graphene oxide nanohybrid electrocatalysts. *Materials Today Energy, 7*, 44–50. Retrieved from https://doi.org/10.1016/j.mtener.2017.11.006

Duan, Z., Wang, P., Yu, G., Liang, M., Dong, J., Su, J., . . . Chen, C. (2021). Aggregation kinetics of UV-aged soot nanoparticles in wet environments: Effects of irradiation time and background solution chemistry. *Water Research*, *201*(6), 117385. Retrieved from https://doi.org/10.1016/j.watres.2021.117385

Dues, C., Schmidt, W. G., & Sanna, S. (2019). Water splitting reaction at polar lithium niobate surfaces. *ACS Omega, 4*(2), 3850–3859. Retrieved from https://doi.org/10.1021/acsomega.8b03271

El-Seedi, H. R., El-Shabasy, R. M., Khalifa, S. A. M., Saeed, A., Shah, A., Shah, R., . . . Guo, W. (2019). Metal nanoparticles fabricated by green chemistry using natural extracts: Biosynthesis, mechanisms, and applications. *RSC Advances*, *9*(42), 24539–24559. Retrieved from https://doi.org/10.1039/c9ra02225b

Garcia, J. L., Miyao, T., Inukai, J., & Tongol, B. J. V. (2022). Graphitic carbon nitride on reduced graphene oxide prepared via semi-closed pyrolysis as electrocatalyst for oxygen reduction reaction. *Materials Chemistry and Physics, 288*, 126415. Retrieved from https://doi.org/10.1016/j.matchemphys.2022.126415

Ghanbari, H., Shafikhani, M. A., & Daryalaal, M. (2019). Graphene nanosheets production using liquid-phase exfoliation of pre-milled graphite in dimethyl formamide and structural defects evaluation. *Ceramics International, 45*(16), 20051–20057. Retrieved from https://doi.org/10.1016/J.CERAMINT.2019.06.267

Gopalakrishnan, V., Radha, K. V., & Devasena, T. (2019). Silver nanoparticles synthesised using *Andrographis paniculata* ameliorates oxidative stress in erythrocyte model. *Materials Research Express*, *6*(8). Retrieved from https://doi.org/10.1088/2053-1591/ab24ea

He, L., Yin, X., Xu, J., Han, H., Li, H., Ren, Q., . . . Xiang, J. (2020). Promoting effects of Fe-Ni alloy on co-production of H_2 and carbon nanotubes during steam reforming of biomass tar over Ni-Fe/α-Al_2O_3. *Fuel*, *276*(1), 118116. Retrieved from https://doi.org/10.1016/j.fuel.2020.118116

Heo, Y. S., Jeon, K. W., Kim, H. M., Park, M. J., Cheon, B. S., Jin, H. D., & Jeong, D. W. (2023). Hydrogen production from waste-derived synthesis gas over Ni(x)Fe(3-x)-CeO_2 catalyst: optimization of Ni/Fe ratio. *International Journal of Hydrogen Energy*, *48*(57), 21752–21764. Retrieved from https://doi.org/10.1016/j.ijhydene.2023.03.007

Hu, X., Zhou, Q., Cheng, P., Su, S., Wang, X., Gao, X., . . . Liu, J. (2019). Nickel-iron selenide polyhedral nanocrystal with optimized surface morphology as a high-performance bifunctional electrocatalyst for overall water splitting. *Applied Surface Science*, *488*(5), 326–334. Retrieved from https://doi.org/10.1016/j.apsusc.2019.05.220

Huo, L., Jin, C., Jiang, K., Bao, Q., Hu, Z., & Chu, J. (2022). Applications of nickel-based electrocatalysts for hydrogen evolution reaction. *Advanced Energy and Sustainability Research, 3*(4), 2100189. Retrieved from https://doi.org/10.1002/aesr.202100189

Khan, A. K., Hano, C., Renouard, S., Drouet, S., Blondeau, J. P., Anjum, I., . . . Anjum, S. (2021). Effect of UV irradiation (A and C) on C*asuarina equisetifolia*-mediated biosynthesis and characterization of antimicrobial and anticancer activity of biocompatible zinc oxide nanoparticles. *Pharmaceutics*, *13*(11). Retrieved from https://doi.org/10.3390/pharmaceutics13111977

Khan, S. B., Kamal, T., Asiri, A. M., & Bakhsh, E. M. (2021). Iron doped nanocomposites based efficient catalyst for hydrogen production and reduction of organic pollutant. *Colloids and Surfaces A: Physicochemical and Engineering Aspects, 608*, 125502. Retrieved from https://doi.org/10.1016/j.colsurfa.2020.125502

Kumar, A., Vikrant, K., Younis, S. A., & Kim, K. H. (2023). Tuning of active nickel species in MOF-derived

nickel catalysts for the control on acetic acid steam reforming and hydrogen production. *International Journal of Hydrogen Energy, 48*(40), 14964–14977. Retrieved from https://doi.org/10.1016/j.ijhydene.2023.01.036

Lian, J., Wu, Y., Zhang, H., Gu, S., Zeng, Z., & Ye, X. (2018). One-step synthesis of amorphous Ni–Fe–P alloy as bifunctional electrocatalyst for overall water splitting in alkaline medium. *International Journal of Hydrogen Energy, 43*(29), 12929–12938. Retrieved from https://doi.org/10.1016/j.ijhydene.2018.05.107

Liang, Z., Ahn, H. S., & Bard, A. J. (2017). A study of the mechanism of the hydrogen evolution reaction on nickel by surface interrogation scanning electrochemical microscopy. *Journal of the American Chemical Society, 139*(13), 4854 – 4858. Retrieved from https://doi.org/10.1021/jacs.7b00279

Nandiyanto, A. B. D., Oktiani, R., & Ragadhita, R. (2019). How to read and interpret ftir spectroscope of organic material. *Indonesian Journal of Science and Technology*, *4*(1), 97–118. Retrieved from https://doi.org/10.17509/ijost.v4i1.15806

Nguyen, N. T. T., Nguyen, L. M., Nguyen, T. T. T., Nguyen, T. T., Nguyen, D. T. C., & Tran, T. Van. (2022). Formation, antimicrobial activity, and biomedical performance of plant-based nanoparticles: A review. *Environmental Chemistry Letters* (Volume 20, Issue 4). New York, NY: Springer International Publishing. Retrieved from https://doi.org/10.1007/s10311-022-01425-w

Paperzh, K., Alekseenko, A., Safronenko, O., Nikulin, A., Pankov, I., & Guterman, V. (2021). UV radiation effect on the microstructure and performance of electrocatalysts based on small Pt nanoparticles synthesized in the liquid phase. *Colloids and Interface Science Communications*, *45*(9), 100517. Retrieved from https://doi.org/10.1016/j.colcom.2021.100517

Park, S., Kim, J., & Kwon, K. (2022). A review on biomass-derived N-doped carbons as electrocatalysts in electrochemical energy applications. *Chemical Engineering Journal*, *446*(P1), 137116. Retrieved from https://doi.org/10.1016/j.cej.2022.137116

Paul, K. K., Sreekanth, N., Biroju, R. K., Narayanan, T. N., & Giri, P. K. (2018). Solar light driven photo electrocatalytic hydrogen evolution and dye degradation by metal-free few-layer MoS_2 nanoflower/TiO_2(B) nanobelts heterostructure. *Solar Energy Materials and Solar Cells*, *185*(4), 364–374. Retrieved from https://doi.org/10.1016/j.solmat.2018.05.056

Rubi, R. V. C., Fabro, M. A., Dela Rosa, M. B., Diongson, M. A. A., Lee, G. H., Mondala, A. R., . . . Hamidah, N. L. (2020). Synthesis and characterization of Ni-Zn-Fe alloy as an electrocatalyst for alkaline water electrolysis. *E3S Web of Conferences, 190*(1), 0036. Retrieved from https://doi.org/10.1051/e3sconf/202019000036

Sangeetha, S., Archit, R., & Sathia Velu, A. (2014). Phytochemical testing, antioxidant activity, HPTLC, and FTIR analysis of antidiabetic plants *Nigella sativa*, *Eugenia jambolana*, *Andrographis paniculata* and *Gymnema sylvestre*. *Research Journal of Biotechnology*, *9*(9), 65–72.

Sapountzi, F. M., Gracia, J. M., Weststrate, C. J. K., Fredriksson, H. O. A., & Niemantsverdriet, J. W. H. (2017). Electrocatalysts for the generation of hydrogen, oxygen and synthesis gas. *Progress in Energy and Combustion Science, 58*, 1–35. Retrieved from https://doi.org/10.1016/j.pecs.2016.09.001

Stratakes, B. M., Dempsey, J. L., & Miller, A. J. M. (2021). Determining the overpotential of electrochemical fuel synthesis mediated by molecular catalysts: Recommended practices, standard reduction potentials, and challenges. *ChemElectroChem, 8*(22), 4161–4180. Retrieved from https://doi.org/10.1002/celc.202100576

Sundrarajan, M., & Muthulakshmi, V. (2021). Green synthesis of ionic liquid mediated neodymium oxide nanoparticles by *Andrographis paniculata* leaves extract for effective bio-medical applications. *Journal of Environmental Chemical Engineering, 9*(1), 104716. Retrieved from https://doi.org/10.1016/j.jece.2020.104716

Tiwari, S. K., Sahoo, S., Wang, N., & Huczko, A. (2020). Graphene research and their outputs: Status and prospect. *Journal of Science: Advanced Materials and Devices, 5*(1), 10–29. Retrieved from https://doi.org/10.1016/j.jsamd.2020.01.006

Watcharaporn, K., Opaprakasit, M., & Pimpan, V. (2014). Effects of UV radiation and pH of tannic acid solution in the synthesis of silver nanoparticles. *Advanced Materials Research, 911*, 110–114. Retrieved from https://doi.org/10.4028/www.scientific.net/AMR.911.110

Wongsa, P., Phatikulrungsun, P., & Prathumthong, S. (2022). FT-IR characteristics, phenolic profiles and inhibitory potential against digestive enzymes of 25 herbal infusions. *Scientific Reports*, *12*(1), 1–11. Retrieved from https://doi.org/10.1038/s41598-022-10669-z

Zhan, J., Lei, Z., & Zhang, Y. (2022). Non-covalent interactions of graphene surface: Mechanisms and applications. *Chem, 8*(4), 947–979. Retrieved from https://doi.org/10.1016/j.chempr.2021.12.015

Zhang C., Xu Z., Han N., Tian Y., Jiang L., (2023). Superaerophilic/ superaerophobic cooperative electrode for efficient hydrogen evolution reaction via enhanced mass transfer. *Science Advances*, *9*(10). doi:10.1126/sciadv.add6978

Zhong, Y., Wang, Z., Guo, Z., & Tang, Q. (2013). Prevention of agglomeration/defluidization in fluidized bed reduction of Fe_2O_3 by CO: The role of magnesium and calcium oxide. *Powder Technology, 241*, 142–148. Retrieved from https://doi.org/10.1016/j.powtec.2013.03.030

Zuo, C., Su, Q., & Yan, X. (2023) Research progress of co-catalysts in photocatalytic CO_2 Reduction: A review of developments, opportunities, and directions. *Processes 2023*, *11*, 867. Retrieved from https://doi.org/10.3390/pr11030867